

# Influence of Irradiation Time, Particle Sizes, and Initial Moisture Content During Microwave Drying of Multi-Layered Capillary Porous Materials

P. Ratanadecho  
K. Aoki  
M. Akahori

Department of Mechanical Engineering,  
Nagaoka University of Technology,  
1603-1, Kamitomioka, Nagaoka,  
Niigata, 940-2188, Japan

*The drying of capillary porous materials by microwave with rectangular waveguide has been investigated numerically and experimentally. Most importantly, it focuses on the investigation of the distributions of electric field, temperature and moisture profiles within the capillary porous materials. The measurements of temperature and moisture distributions within the capillary porous materials provide a good basis for understanding of the microwave drying process. The mathematical model gives qualitatively comparable trends to experimental data. The calculations of electromagnetic fields inside the rectangular waveguide and the capillary porous materials show that the variation of particle sizes and initial moisture content changes the degree of penetration and rate of microwave power absorbed within the sample. Further, the small particle size leads to much higher capillary pressure resulting in a faster drying time. [DOI: 10.1115/1.1423951]*

*Keywords:* Electromagnetic, Heat Transfer, Microwave, Moisture, Numerical Methods, Packed Beds, Porous Media

## 1 Introduction

A convenient starting point of drying theory is a recent work by Whitaker [1], who derived locally volume averaged conservation equations for two-phase capillary flow in porous media. In the past decade, microwave technology has been applied to many processes. Microwave drying is one of the most interesting methods for drying materials. Unlike other heat sources such as conventional heating, where heat is applied externally to the surface of the material, microwave irradiation penetrates and simultaneously heats the bulk of the material. When properly designed, microwave drying systems have several advantages over conventional mechanical methods, such as reducing the drying times, high energy efficiency, and offer improvements in product quality for various industrial applications (Feng et al. [2] and Feng et al. [3]).

Microwave radiations have typical wavelengths and a penetration depth of roughly the same order of magnitude, commensurate with the size of the sample to be dried. For instance, the wavelength of an electromagnetic at frequency of 2.45 GHz is 12.4 cm and the penetration depth, that is the distance from the surface of the sample at which the power drop to  $e^{-1}$  from its initial value, is 2 cm of water at 60°C. Thus, a volumetric heat source is dissipated through the sample due to the characteristic of dielectric losses [4]. Further, the moisture and temperature distributions for microwave drying can appear to have uniform shapes, due to this phenomenon.

There are many successful examples of microwave application, including the drying of foods, drying of textiles, freeze drying process, and vulcanizations of rubber. Metaxas and Meredith [5] provide good introduction to heat and mass transfers in micro-

wave processing. A number of other analyses of microwave heating processes have appeared in the recent literatures (Ayappa et al. [6], Li et al. [7] and Clemens et al. [8]). The one-dimensional analysis for heat and mass transport during microwave drying in porous material has been studied by Gori et al. [9], Perkin et al. [10] and Turner et al. [11].

Of all models above, the microwave power absorbed was assumed to decay exponentially into the sample following the Lambert's law. However, this assumption is valid for the large dimension samples (depth of bed,  $d_p \approx 2.7 \times$  penetration depth) [12,13]. For the small samples heat in a faster rate by microwave due to the resonance of standing waves whereas resonance is completely absent for greater length scales. In perspective, Lambert's exponential decay law cannot predict resonance. Therefore, the spatial variations of the electromagnetic field within small samples must be obtained by solution of the Maxwell's equations [14].

The two-dimensional models of interaction between electromagnetic field and dielectric materials have been used previously to study numerous heating processes in a variety of microwave applicator configurations such as rectangular waveguide and cavities ([14–16]). However, previous investigation considered only a single-layer sample. Indeed, little effort has been reported on the study of drying process of multi-layered materials in microwave fields, especially a complete comparison between mathematical. In this work, samples in a microwave cavity of 2.45 GHz and TE<sub>10</sub> mode were packed beds of glass beads and water. The effects of the irradiation time, particle sizes and the variation of initial moisture content on microwave drying kinetics at long stages of drying process were clarified in detail. The result presented here provides a basis for fundamental understanding of microwave drying of capillary porous materials.

## 2 Experimental Apparatus

Figure 1 shows the experimental apparatus used. The microwave system was a monochromatic wave of TE<sub>10</sub> mode operating

Contributed by the Heat Transfer Division for publication in the JOURNAL OF HEAT TRANSFER. Manuscript received by the Heat Transfer Division April 10, 2001; revision received September 10, 2001. Associate Editor: H. Bau.

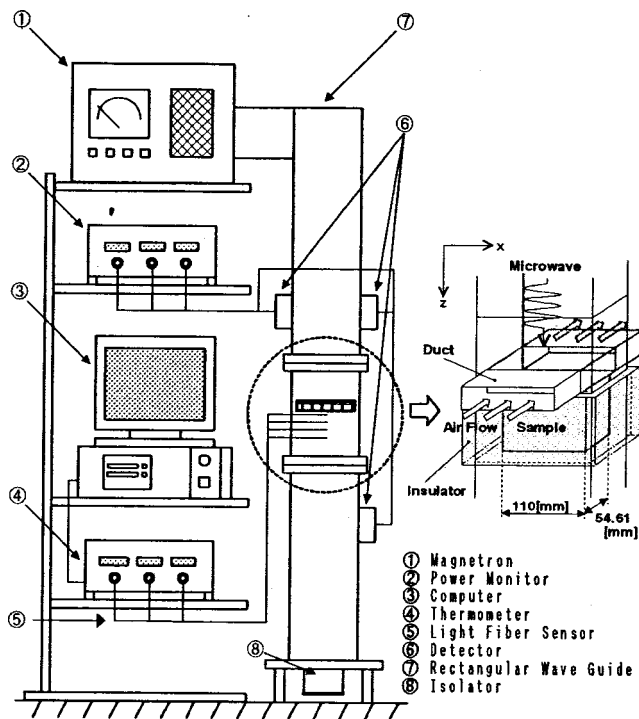


Fig. 1 Schematic of experimental facility: (a) equipment setup; and (b) multi-layered porous packed bed (Sample)

at a frequency of 2.45 GHz. Microwave energy was generated by magnetron (Micro Denshi Co., model UM-1500, Tokyo, Japan), it was transmitted along the  $z$ -direction of the rectangular waveguide with inside dimensions of 110 mm  $\times$  54.61 mm toward a water load that was situated at the end of the waveguide. The water load (lower absorbing boundary) ensured that only a minimal amount of microwave was reflected back to the sample. Also, an isolator (upper absorbing boundary) was used to trap any microwave reflected from the sample to prevent it from damaging the magnetron. Output of magnetron was adjusted at 50 W. The powers of incident, reflected and transmitted waves were measured by a wattmeter using a directional coupler (Micro Denshi Co., model DR-5000, Tokyo, Japan).

As shown in Fig. 1(b), the samples were porous packed bed, which compose of glass beads and water. A sample container was made from polypropylene with a thickness of 0.75 mm, it did not absorb microwave energy. In this study, the voids occupy from a fraction up to 38 percent of the whole volume of packed beds. The samples were prepared in two configurations: a single-layered packed bed ( $d=0.15$  mm,  $d=1.0$  mm, and  $d_p=50$  mm) and a two-layered packed bed, respectively. In the case of two-layered packed bed was classified in two configurations: F-C bed (attach-

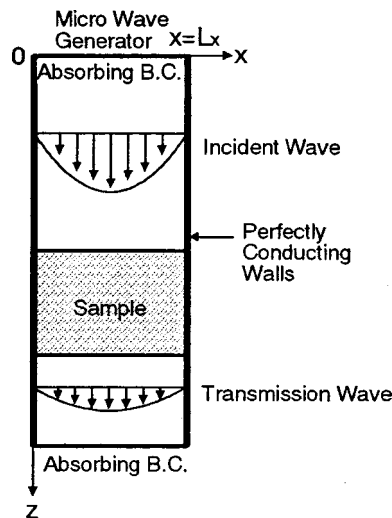


Fig. 2 Physical model

ing fine bed ( $d=0.15$  mm,  $d_p=12.5$  mm) on coarse bed ( $d=0.4$  mm,  $d_p=22.5$  mm)), and C-F bed (attaching fine bed ( $d=0.15$  mm,  $d_p=22.5$  mm) under coarse bed ( $d=0.4$  mm,  $d_p=22.5$  mm)), respectively. The sample of packed bed was inserted in the rectangular waveguide. The distributions of temperature within the sample were measured using fiberoptic (LUXTRON Fluoroptic Thermometer, Model 790, Santa Clara, Canada, accurate to  $\pm 0.5^\circ\text{C}$ ), which were placed in the center of the sample at each 5 mm interval. An infrared camera was also used to measure the distributions of temperature within the sample in  $x$ - $z$  plane. In each test run, the weight loss of the sample was measured by mass scale with high precision. The water saturations in the packed bed were defined as the fraction of the volume occupied by water to volume of the pores. They were obtained by weighing dry and wet mass of the sample which were cut out in volume (four positions) of about 110 mm  $\times$  54.61 mm  $\times$  12.5 mm at the end of each run. The water saturation formula can be described in the following form:

$$s = \frac{\rho_p(1 - \phi)(m_w - m_d)}{\rho_l \phi m_d} \quad (1)$$

where  $s$  is water saturation,  $m_w$  and  $m_d$  are wet and dry mass of the sample, respectively,  $\phi$  is porosity,  $\rho_l$  and  $\rho_p$  are densities of water and particle, respectively. During the experimental microwave drying processes, the uncertainty of our data might come from the variations in humidity, room temperature and human errors. The uncertainty in drying kinetics was assumed to result from errors in the measured weight of the sample. The calculated drying kinetic uncertainties in all tests were less than 3 percent. The uncertainty in temperature was assumed to result from errors in measured input power, ambient temperature and ambient humidity. The calculated uncertainty associated with temperature was less than 2.85 percent.

### 3 Analysis of Mathematical Modeling

**3.1 Analysis of Electromagnetic Model.** Figure 2 shows the physical model used for analyzing microwave drying of capillary porous materials in a rectangular waveguide. The proposed model is based on the following assumptions: (1) since the microwave field in the  $\text{TE}_{10}$  mode has no variation of field in the direction between the broad faces, a two-dimensional model over the  $x$ - $z$  plane is applicable to analysis of electromagnetic field inside a rectangular waveguide [14]; (2) the absorption of microwave energy by the cavity (including air) in the rectangular waveguide is negligible; (3) the walls of a rectangular waveguide are perfect

conductors; and (4) The effect of the sample container (made of polypropylene) on the electromagnetic field can be neglected because it did not absorb microwave energy.

**Basic Equations.** The basic equations for the electromagnetic field are based on the well-known Maxwell relations. For the microwave of TE<sub>10</sub> mode [14], the governing equations can be written in term of the component notations of electric and magnetic field intensities:

$$\frac{\partial E_y}{\partial z} = \mu \frac{\partial H_x}{\partial t} \quad (2)$$

$$\frac{\partial E_y}{\partial x} = -\mu \frac{\partial H_z}{\partial t} \quad (3)$$

$$-\left(\frac{\partial H_z}{\partial x} - \frac{\partial H_x}{\partial z}\right) = \sigma E_y + \varepsilon \frac{\partial E_y}{\partial t} \quad (4)$$

where

$$\varepsilon = \varepsilon_0 \varepsilon_r, \quad \mu = \mu_0 \mu_r, \quad \sigma = 2\pi f \varepsilon \tan \delta. \quad (5)$$

In this study, the effects on the overall drying kinetics are examined by selecting the dielectric properties as a function of moisture content and temperature. In order to determine the functional dependence of the combination of moisture content and temperature, the theory surrounding mixing formulas is used [17], in which the volume fractions ( $v$ ) of water saturation, water vapor and glass particle were considered, as follows:

$$\varepsilon_r(s, T) = (\varepsilon'_r(s, T) - j\varepsilon''_r(s, T)) \quad (6)$$

where

$$[\varepsilon'_r(s, T)]^m = \sum_{i=1}^3 v_i [\varepsilon'_{ri}(T)]^m = \phi s [\varepsilon'_{rl}(T)]^m + \phi(1-s) [\varepsilon'_{ra}]^m + (1-\phi) [\varepsilon'_{rp}]^m \quad (7)$$

$$[\varepsilon''_r(s, T)]^m = \sum_{i=1}^3 v_i [\varepsilon''_{ri}(T)]^m = \phi s [\varepsilon''_{rl}(T)]^m + \phi(1-s) [\varepsilon''_{ra}]^m + (1-\phi) [\varepsilon''_{rp}]^m. \quad (8)$$

In above equations, the parameter  $m$  is likely to vary over the range 0–1, as suggested by Wang and Schmutge [17]. A value of  $m=0.33$  has been used throughout in this study. The loss tangent coefficient can be expressed as follow:

$$\tan \delta = \frac{\varepsilon''_r(s, T)}{\varepsilon'_r(s, T)}. \quad (9)$$

**Boundary Conditions.** Corresponding to the physical model shown in Fig. 2, boundary conditions are given in the following list.

- (a) Perfectly conducting boundaries; boundary conditions on the inner wall surface of a rectangular waveguide are given by using Faraday's law and Gauss' theorem:

$$E_t = 0, \quad H_n = 0. \quad (10)$$

- (b) Continuity boundary condition; boundary conditions along the interface between different materials, for example between air and dielectric material surface, are given by using Ampere's law and Gauss' theorem:

$$E_t = E'_t, \quad H_t = H'_t, \quad D_n = D'_n, \quad B_n = B'_n. \quad (11)$$

- (c) Absorbing boundary condition; at both ends of the rectangular waveguide, the first order absorbing conditions proposed by Mur [18] are applied:

$$\frac{\partial E_y}{\partial t} = \pm v \frac{\partial E_y}{\partial z}. \quad (12)$$

Here, the symbol  $\pm$  represents forward or backward waves and  $v$  is phase velocity of the microwave.

Oscillation of the electric and magnetic field intensities by magnetron; incident wave due to magnetron is given by the following equations:

$$E_y = E_{yin} \sin\left(\frac{\pi x}{L_x}\right) \sin(2\pi f t), \quad H_x = \frac{E_{yin}}{Z_H} \sin\left(\frac{\pi x}{L_x}\right) \sin(2\pi f t). \quad (13)$$

$Z_H$  is the wave impedance defined as

$$Z_H = \frac{\lambda_g Z_I}{\lambda} = \frac{\lambda_g}{\lambda} \sqrt{\frac{\mu}{\varepsilon}}. \quad (14)$$

**3.2 Analysis of Heat and Mass Transport Models.** A schematic diagram of model is shown in Fig. 2. By conservations of mass and energy in the sample, the governing equation of mass and energy for all phases can be derived by using the volume average technique. The main transport mechanisms that enable moisture movement during microwave drying of sample are: liquid flow driven by capillary pressure gradient and gravity while the vapor is driven by the gradient of the partial pressure of the evaporating species. In this study, several simplifying assumptions are made in order to obtain a closed set of governing macroscopic equations: (1) the capillary porous material is rigid, no chemical reactions take place in the sample; (2) local thermodynamic equilibrium is assumed; (3) simultaneous heat and mass transport occurs at a constant pressure, where the dominant mechanisms are capillary transport, vapor diffusion and gravity; such is generally the case in drying of capillary porous medium at atmospheric pressure when the temperature is lower than the boiling point [19]; (4) the gas binary mixture of air and water vapor behaves like an ideal gas; and (5) corresponding to electromagnetic field, temperature and moisture profiles also can be assumed to be two-dimensional in the  $x$ - $z$  plane.

**Basic Equations.** The governing equations based on a volume average approach led to the following conservation equations describing the drying process of capillary porous materials:

**Mass Conservation.**

$$\phi \frac{\partial}{\partial t} \{\rho_l s + \rho_v(1-s)\} + \frac{\partial}{\partial x} [\rho_l u_l + \rho_v u_v] + \frac{\partial}{\partial z} [\rho_l w_l + \rho_v w_v] = 0 \quad (15)$$

**Energy Conservation.**

$$\begin{aligned} & \frac{\partial}{\partial t} [(\rho c_p)_T T] + \nabla \cdot \{[\rho_l c_{pl} \mathbf{u}_l + (\rho_a c_{pa} + \rho_v c_{pv}) \mathbf{u}_g] T\} + H_v \dot{n} \\ & = -\nabla q + Q, \end{aligned} \quad (16)$$

where  $Q$  is the microwave power absorbed term, which is a function of the electric field and defined as [8]:

$$Q = 2\pi \cdot f \cdot \varepsilon_0 \cdot \varepsilon_r (\tan \delta) E_y^2 \quad (17)$$

**Phenomenological Relations.**

In order to complete the system of equations, the expressions for the superficial average velocity of the liquid and gas phases the generalized Darcy's law in the following vector form is used:

$$\mathbf{u}_l = -\frac{KK_{rl}}{\mu_l} [\nabla p_g - \nabla p_c - \rho_l \mathbf{g}], \quad \mathbf{u}_g = -\frac{KK_{rg}}{\mu_g} [\nabla p_g - \rho_g \mathbf{g}] \quad (18)$$

the velocity of vapor water and air phase the generalized Fick's law for a two-component gas mixture can be expressed in vector form as

$$\rho_v \mathbf{u}_v = \rho_v \mathbf{u}_g - \rho_g D_m \nabla \left(\frac{\rho_v}{\rho_g}\right), \quad \rho_a \mathbf{u}_a = \rho_a \mathbf{u}_g - \rho_g D_m \nabla \left(\frac{\rho_a}{\rho_g}\right), \quad (19)$$

where  $D_m$  is the effective molecular mass diffusion [20]:

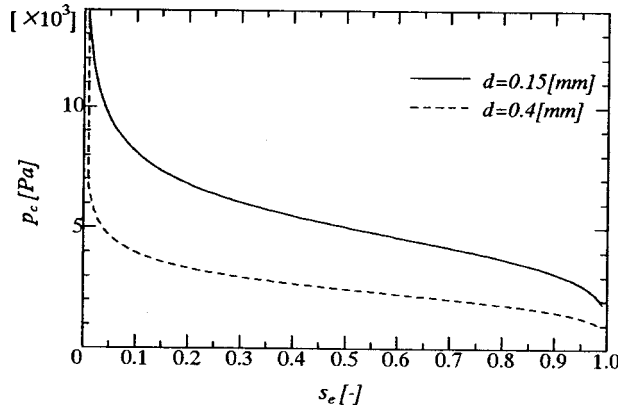


Fig. 3 Typical relationship between,  $p_c$  and  $s_e$

$$D_m = \frac{2\phi}{3-\phi}(1-s)D_0. \quad (20)$$

Fourier's law is used to define the heat flux through the porous materials

$$q = -\lambda_{\text{eff}} \nabla T \quad (21)$$

Equilibrium Relations.

The system of conservation equations obtained for multiphase transport mode requires constitutive equation for relative permeabilities  $K_r$ , capillary pressure  $p_c$ , capillary pressure functions or Leverett functions  $J(s_e)$ , and the effective thermal conductivity  $\lambda_{\text{eff}}$ . A typical set of constitutive relationships for liquid and gas system given by [21]

$$K_{rl} = s_e^3, \quad K_{rg} = (1-s_e)^3, \quad (22)$$

where  $s_e$  is the effective water saturation considered the irreducible water saturation  $s_{ir}$  and defined by

$$s_e = \frac{s - s_{ir}}{1 - s_{ir}}. \quad (23)$$

The capillary pressure  $p_c$  is further assumed to be a function of water saturation or Leverett functions  $J(s_e)$  and surface tension  $\xi(T)$ . The Leverett functions  $J(s_e)$  is dependent on the internal structure of the porous materials and defined by [22]:

$$J(s_e) = 0.325(1/s_e - 1)^{0.217}. \quad (24)$$

The relationship between the capillary pressure and the water saturation is defined by using Leverett functions  $J(s_e)$ :

$$p_c = p_g - p_l = \frac{\xi(T)}{\sqrt{K/\phi}} J(s_e). \quad (25)$$

Figure 3 shows the typical moisture characteristic curve for different particle sizes obtained from present experiments. It is seen that, in the case of the same water saturation, a smaller particle size corresponds to a higher capillary pressure.

Based on the experimental results of Aoki et al. [22] using a glass beads unsaturated with water, the effective thermal conductivity is further assumed to be a function of water saturation and defined by

$$\lambda_{\text{eff}} = \frac{0.8}{1 + 3.78e^{-5.95s}} \quad (26)$$

After some mathematical manipulations, the two-dimensional systems of two non-linear coupled partial differential equations which govern the microwave drying process are given by

Moisture Transport Equation.

$$\begin{aligned} \phi \frac{\partial}{\partial t} \{ \rho_l s + \rho_v (1-s) \} + \frac{\partial}{\partial x} \left[ \rho_l \frac{KK_{rl}}{\mu_l} \left( \frac{\partial p_c}{\partial x} \right) - D_m \frac{\partial \rho_v}{\partial x} \right] \\ + \frac{\partial}{\partial z} \left[ \rho_l \frac{KK_{rl}}{\mu_l} \left( \frac{\partial p_c}{\partial z} + \rho_l g_z \right) + \rho_v \frac{KK_{rg}}{\mu_g} (\rho_g g_z) - D_m \frac{\partial \rho_v}{\partial z} \right] \\ = 0 \end{aligned} \quad (27)$$

Heat Transport Equation.

$$\begin{aligned} \frac{\partial}{\partial t} [(\rho C_p)_T T] + \frac{\partial}{\partial x} [ \{ \rho_l C_{pl} u_l + (\rho_a C_{pa} + \rho_v C_{pv}) u_g \} T ] \\ + \frac{\partial}{\partial z} [ \{ \rho_l C_{pl} w_l + (\rho_a C_{pa} + \rho_v C_{pv}) w_g \} T ] + H_v \dot{n} \\ = \frac{\partial}{\partial x} \left[ \lambda_{\text{eff}} \frac{\partial T}{\partial x} \right] + \frac{\partial}{\partial z} \left[ \lambda_{\text{eff}} \frac{\partial T}{\partial z} \right] + Q, \end{aligned} \quad (28)$$

where  $(\rho C_p)_T$  is the effective heat capacitance of water-gas-matrix mixtures:

$$(\rho C_p)_T = \rho_l C_{pl} \phi s + \{ (\rho C_p)_a + (\rho C_p)_v \} \phi (1-s) + \rho_p C_{pp} (1-\phi). \quad (29)$$

Also, the phase change term is given by

$$\begin{aligned} \dot{n} = \frac{\partial}{\partial t} \{ \rho_v \phi (1-s) \} + \frac{\partial}{\partial x} \left[ -D_m \frac{\partial \rho_v}{\partial x} \right] \\ + \frac{\partial}{\partial z} \left[ \rho_v \frac{KK_{rg}}{\mu_g} \rho_g g_z - D_m \frac{\partial \rho_v}{\partial z} \right]. \end{aligned} \quad (30)$$

Boundary and Initial Conditions.

The boundary conditions proposed for the exchange of energy and mass at the open boundary can be described in the following form:

$$-\lambda \frac{\partial T}{\partial z} = h_c (T - T_a) + \dot{n} H_v \quad (31)$$

$$\rho_l w_l + \rho_v w_v = h_m (\rho - \rho_a). \quad (32)$$

Considering the boundary conditions at the closed boundary that no heat and mass exchange take place

$$\frac{\partial T}{\partial x} = \frac{\partial T}{\partial z} = 0, \quad \frac{\partial u}{\partial x} = \frac{\partial w}{\partial z} = 0. \quad (33)$$

The initial conditions are given by uniform initial temperature and moisture content.

#### 4 Numerical Procedure

In order to predict the electromagnetic field (Eqs. (2)–(4)), a finite difference time domain (FDTD) method is applied. The system of nonlinear partial differential equations (Eqs. (27)–(33)) was solved by the method of finite differences based on the notion of control volumes as described by Patankar [23]. The Newton-Raphson method was employed at each iteration to quicken the convergence. Initially, the temperature and moisture profiles were set to be equal at all nodes at values corresponding to the measured capillary porous medium conditions. Considering the microwave drying in TE<sub>10</sub> mode, it is the lowest mode of the supported microwave field for waves transmitted in the present rectangular waveguide without power dissipation. The type of wave mode is prescribed by the frequency and waveguide dimensions. Spatial and temporal resolution was selected to ensure of stability and accuracy. To insure stability of the time-stepping algorithm,  $\Delta t$  was chosen to satisfy the Courant stability condition [15]:

$$\Delta t \leq \frac{\sqrt{(\Delta x)^2 + (\Delta z)^2}}{v} \quad (34)$$

**Table 1** The electromagnetic and thermo physical properties used in the computations [25]

$\epsilon_0 = 8.85419 \times 10^{-12} [\text{F/m}]$	$\mu_0 = 4.0\pi \times 10^{-7} [\text{H/m}]$	
$\epsilon_{r0} = 1.0,$	$\epsilon_{rp} = 5.1$	
$\mu_{r0} = 1.0,$	$\mu_{rp} = 1.0,$	
$\tan \delta_0 = 0.0,$	$\tan \delta_p = 0.01$	$\mu_{rl} = 1.0$
$\rho_0 = 1.20 [\text{kg/m}^3],$	$\rho_p = 2500 [\text{kg/m}^3],$	$\rho_l = 1000 [\text{kg/m}^3]$
$C_{p0} = 1.00 [\text{kJ}/(\text{kg K})],$	$C_{pp} = 0.8 [\text{kJ}/(\text{kg K})],$	$C_{pl} = 4.18 [\text{kJ}/(\text{kg K})]$
$\epsilon_{rl} = 88.15 - 0.414T + (0.131 \times 10^{-2})T^2 - (0.046 \times 10^{-4})T^3$		
$\tan \delta_l = 0.323 - (9.499 \times 10^{-3})T + (1.27 \times 10^{-4})T^2 - (6.13 \times 10^{-7})T^3$		

and the spatial resolution of each cell defined as

$$\Delta x, \Delta z \leq \frac{\lambda_g}{10\sqrt{\epsilon_r}} \tag{35}$$

Corresponding to Eqs. (34) and (35), the calculation conditions were as follows: (1) because the propagating velocity of microwave is very fast compared with the rate of heat transfer, different time steps of  $dt = 1$  [ps] and  $0.1$  [s] were used for the computation of the electromagnetic field and temperature profile: the spatial step size is  $dx = dz = 1.0$  [mm]; (2) number of grid:  $N = 110$  (width)  $\times 200$  (length); and (3) relative errors in the iteration procedure of  $10^{-8}$  were chosen. One aspect of model verification was to compare drying data from experiments run under different conditions with mathematical simulations using parameter values obtained from Table 1.

## 5 Results and Discussion

**5.1 Simulation of Electric Field Inside a Rectangular Waveguide.** In the beginning, to understand the detailed structures of electric field developed inside a rectangular waveguide, the numerical simulation of the following three cases are conducted: (1) rectangular waveguide is empty, its dielectric constant is unity (which corresponds to that of air); (2) rectangular waveguide is filled with sample (single-layered packed bed) with drying times of 15 min (early drying times); and (3) rectangular waveguide is filled with sample (single-layered packed bed) with drying times of 540 min (long drying times).

Figures 4–6 are the numerical simulation of electric field in TE<sub>10</sub> mode along the center axis ( $x = 54.61$  mm) of rectangular waveguide after 10,000 time steps. In the figures, the vertical axis represents the intensity of the electric field  $E_y$ , which is normalized to the amplitude of the input electromagnetic wave,  $E_{yin}$ .

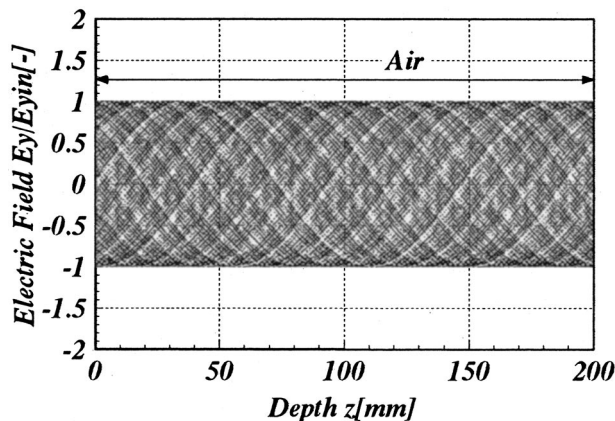


**Fig. 4** Distribution of electric field for case of a rectangular waveguide is empty ( $x = 54.61$  mm)

Figure 4 shows the stationary wave inside the rectangular waveguide with completely absorbed power at the end of the rectangular waveguide (case 1). It is observed that a uniform wave is formed inside a rectangular waveguide. Figure 5 shows the wave distribution of the electric field when a dielectric material or sample is inserted in the rectangular waveguide (case 2). Within the sample, the electric field attenuates owing to energy absorption, and thereafter the absorbed energy is converted to the thermal energy, which increases the sample temperature. In the figure, the electric field with a small amplitude is formed within the sample waveguide. Furthermore, focusing attention of field pattern outside the sample (left hand side), a stronger standing wave with a larger amplitude is formed by interference between the forward wave and waves reflected from the surface of sample due to the different of dielectric properties of material (air and sample)

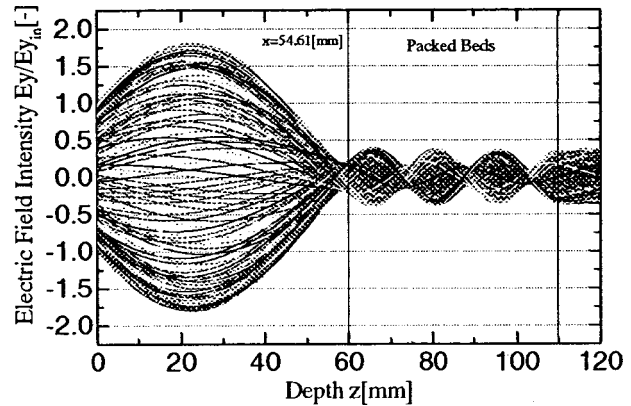


**Fig. 5** Distribution of electric field for the sample inserted in the rectangular waveguide ( $t = 15$  min,  $x = 54.61$  mm)

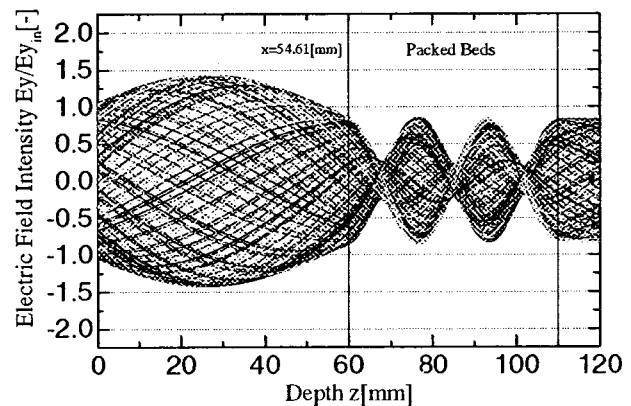
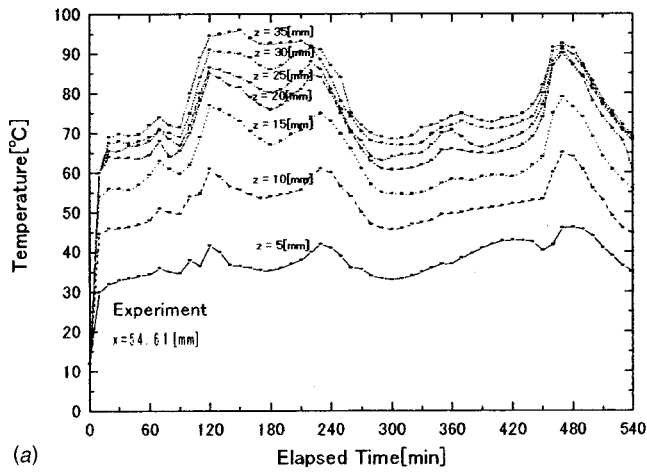
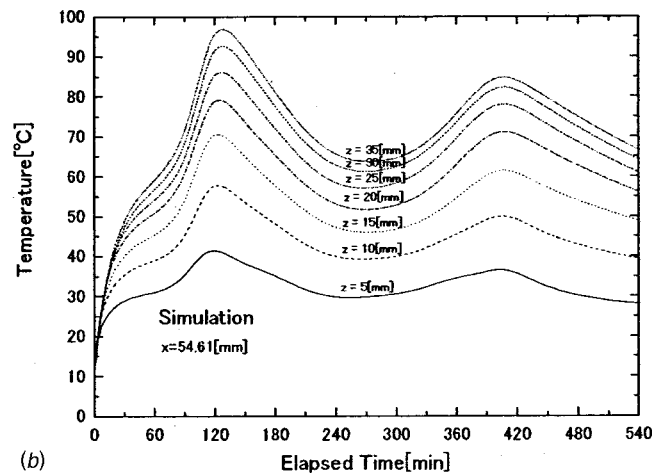


**Fig. 6** Distribution of electric field for the sample inserted in the rectangular waveguide ( $t = 540$  min,  $x = 54.61$  mm)



(a)



(b)

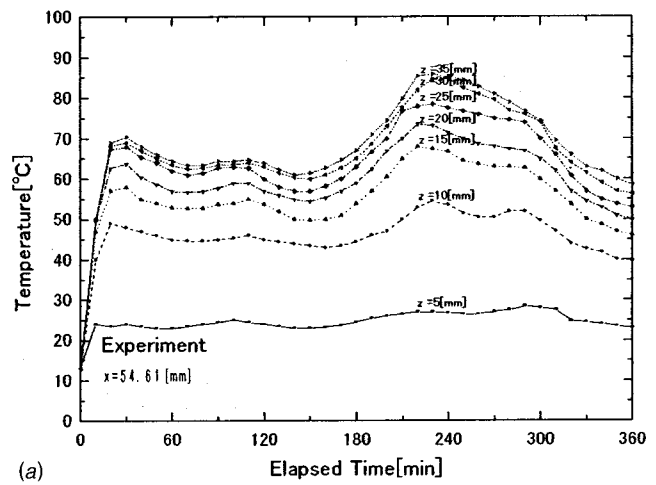
Fig. 7 Temperature profile in times at various depths ( $P=50$  W,  $d=0.15$  mm,  $s_0=1.0$ ): (a) experiment; and (b) simulation

at this surface. Figure 6 shows the wave distribution of the electric field when a dielectric material or sample is inserted in the rectangular waveguide (case 3). In this case after a majority of the moisture level inside the sample has been removed, the effect of wave reflected from the surface of the sample is reduce which increases the large part of microwaves inside the sample. Consequently, the reflection and transmission components at each interface will contribute to the resonance of standing wave configuration with the larger amplitude and wave length inside the sample where the moisture content is small in comparison with previous cases.

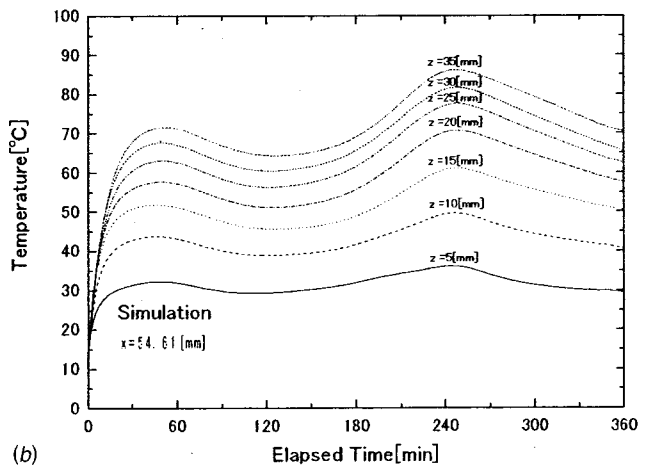
## 5.2 Microwave Drying of Single-Layered Porous Packed Bed

*The Distribution of Temperature Profiles Within the Sample.* The predicted results are compared with experimental microwave drying data in Figs. 7–9, which corresponds to that of  $T_0 = 10.4^\circ\text{C}$ ,  $T_a = 10.4^\circ\text{C}$ , and  $P = 50$  W, along with the center axis ( $x = 54.61$  mm) of rectangular waveguide.

Figure 7(a) shows the temperature profiles measured by fiberoptic at various times and locations in the case of  $s_0 = 1.0$  and  $d = 0.15$  mm ( $\phi = 0.385$ ). In contrast to that in conventional drying, microwave drying gives higher temperatures inside the drying sample while the surface temperature stays colder due to the cooling effect of surrounding air. At the same time the evaporation takes place at the surface of the sample at a lower temperature due to evaporative cooling. It is seen that the temperature profiles



(a)



(b)

Fig. 8 Temperature profile in times at various depths ( $P=50$  W,  $d=0.15$  mm,  $s_0=0.6$ ): (a) experiment; and (b) simulation

within the sample rise up steadily in the early stages of drying (about 90 min). Due to the large initial moisture content, the skin-depth heating effect causes a majority of microwave to be reflected from the surface during early irradiation stage (as referred to Fig. 5) resulting in a lower rate of microwave power absorbed in the interior (Fig. 10). As the drying process proceeds (about

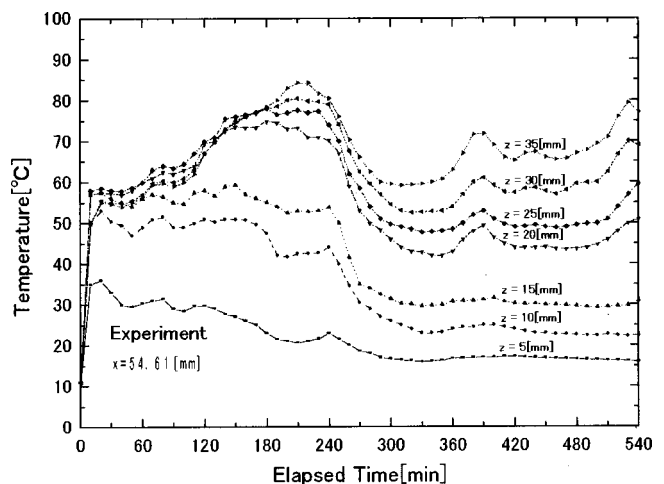


Fig. 9 Temperature profile in times at various depths (Experiment:  $P=50$  W,  $d=1.0$  mm,  $s_0=1.0$ )

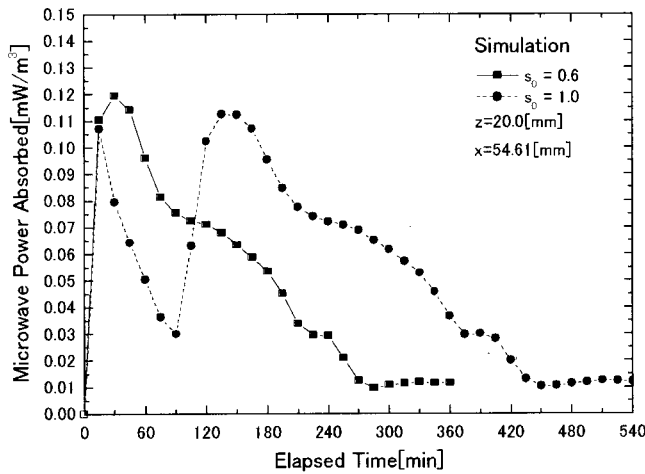
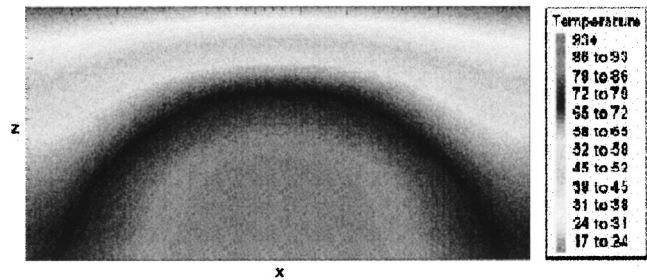


Fig. 10 Microwave power absorbed profile in times: (Simulation  $P=50\text{ W}$ ,  $d=0.15\text{ mm}$ )

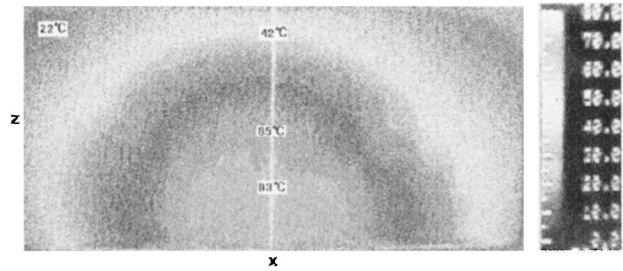
90–240 min), after a majority of moisture content is removed from the sample, the microwave can penetrate further into the sample as material dries (as referred to Fig. 6) where the strength of the microwave power absorbed increases (Fig. 10). During this stage of drying, the behavior of dielectric properties is influenced primarily by that of moisture content, and heating becomes more volumetric. In time about 240 minutes, the temperature starts to drop, this is mainly due to fact that the moisture inside the sample is significantly reduced, reducing dielectric loss factor as well as microwave power absorbed (Fig. 10). However, at long stages of drying (about 480 min), the temperature increases rapidly due to the characteristic of dielectric loss factor, which becomes to dominant microwave drying at low moisture content where the stronger standing wave with a larger amplitude established within the sample [16], [24]. Nevertheless, near the end stages of drying as the majority of moisture content inside the sample is removed, this decreases the microwave power absorbed. Thus, equilibrium is reached between microwave drying and convective losses by lowering the sample temperature.

Figure 8(a) shows the temperature profiles measured by fiberoptic at various times and locations in the case of  $s_0=0.6$  and  $d=0.15\text{ mm}$  ( $\phi=0.385$ ). The temperature profiles within the sample rise up rapidly in the early stages of drying (about 27 min). This is because of the total rate of reflection wave is small in the early stages of drying, and a large part of microwave penetrates into the sample. Such pattern can lead to a much higher rate of microwave power absorbed in the interior compared with a previous case (Fig. 10). Later, the temperature starts to drop continuously since the rate of microwave absorption is lower after a majority of moisture content is removed from the sample. As the drying process proceeds (about 240 minutes) it would eventually cause the temperature level to increase again due to the characteristics of the dielectric loss factor that were explained in Fig. 7.

Figure 9 shows the temperature profiles measured by fiberoptic at various times and locations in the case of  $s_0=1.0$  and  $d=1.0\text{ mm}$ . As the drying proceeds, the temperature profiles within the sample are different from those shown in Fig. 7. In this case, the temperature profiles have a rather unusual shape. This is because of the large particle size corresponding to a lower capillary pressure, the liquid water supply to surface by capillary action becomes insufficient to replace the liquid being evaporated. The latter arises from the fact that the drying layer took place on a front retreating from the surface into the interior of the sample. Furthermore, the combinations of hydrodynamic properties and dielectric properties cause a change in the location of the maximum temperature to occur, especially at the drying times about 45 min–180 min. This trend is more remarkable for large



(a)



(b)

Fig. 11 Comparison between simulated results (a) and experimental results (b) of temperature distribution ( $^{\circ}\text{C}$ ) within the sample ( $s_0=1.0$ ,  $t=120\text{ min}$ ,  $d=0.15\text{ mm}$ , dimensions:  $110\text{ mm}$  ( $x$ )  $\times 50\text{ mm}$  ( $z$ ))

particle sizes having a lower capillary pressure. However, the vapor diffusion becomes strongly effective on the drying kinetics of the large particle sizes. Unfortunately, the lack of experimental data (permabilities and capillary pressure functions) for a large particle sizes so that, the drying kinetics predicted by the mathematical model were unrepresentative.

Additionally, it is evident from the results that the dielectric loss factor can become significant when microwave energy is utilized. The magnitude of this variable will directly affect the amount of microwave power absorbed within the sample during microwave drying process (Fig. 10). Further, for a more complete discussion on the evolution of the dielectric properties as a function of temperature and moisture content (Eqs. (6)–(9)), the reader is referred to Ratanadecho et al. [13].

The observation of temperature profiles depicted in Fig. 7 and Fig. 8 for the sample verify that the match between the experimental data (Fig. 7(a) and Fig. 8(a)) and simulated results (Fig. 7(b) and Fig. 8(b)) is qualitatively consistent, with the simulated results exhibiting the same overall trend of the experimental profiles. However, a fine wavy of the temperature distribution in the experimental results does not appear in the simulated results (Fig. 7(a) and Fig. 7(b)). The discrepancy may be attributed to uncertainties in the thermal and dielectric property database. Additionally, the discrepancy may be attributed from the nonuniformity of the microwave irradiation during experimental process.

Furthermore, the simulation and experimental data (measured by infrared camera) of temperature distributions within the sample in the vertical plane ( $x$ - $z$ ) are compared in Fig. 11 and Fig. 12. The results show the greatest temperature in the center of heating sample where the electric field is maximum for this standing wave configuration, while the outer edges display the lower temperature. It can be seen that the agreement between the two heating patterns is good, particularly concerning the location of the hot region.

*The Distribution of Moisture Profiles Within the Sample.* Figures 13 and 14 show the comparison between simulated results and experimental results (the method of measuring as referred to

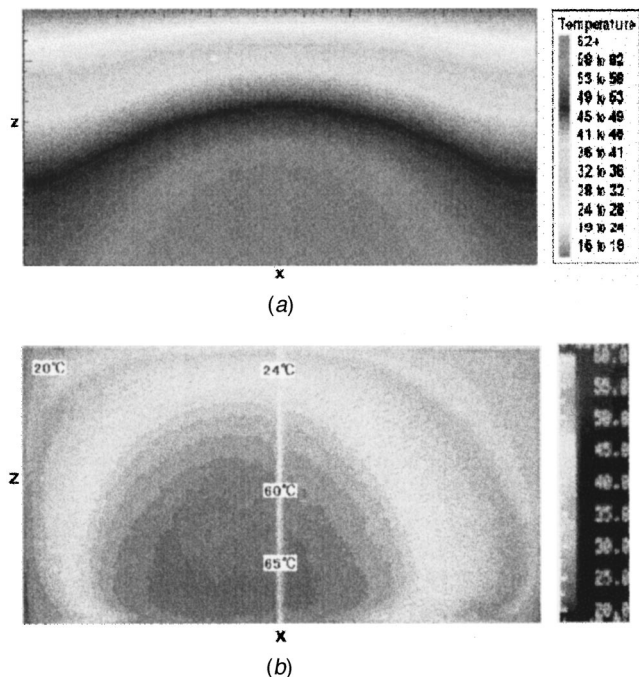


Fig. 12 Comparison between simulated results (a) and experimental results (b) of temperature distribution ( $^{\circ}\text{C}$ ) within the sample ( $s_0=0.6$ ,  $t=120$  min,  $d=0.15$  mm, dimensions: 110 mm ( $x$ )  $\times$  50 mm ( $z$ ))

section 2) of moisture profiles in the case of  $s_0=1.0$  and  $s_0=0.6$ , respectively, which correspond to that of  $T_0=10.7^{\circ}\text{C}$ ,  $T_a=10.7^{\circ}\text{C}$ , and  $P=50$  W.

Figure 14 shows the moisture profile in the case of  $s_0=1.0$  and  $d=0.15$  mm. In the early stages of drying, the moisture content at the leading edge of the sample is lower than that inside the sample, where the moisture decreases due to the gravitational effect. Because of the higher moisture content within the sample, much larger reflected waves develop at the surface during the early stages of the drying. Later, the internal movement of moisture is due to liquid flow by capillary action and vapor flow by molecular diffusion. Liquid phase migration is related to capillary pressure gradient as well as temperature (which corresponds to that of surface tension, as referred to Eq. (25)), whereas in the vapor phase is driven by the gradient of the partial pressure of the

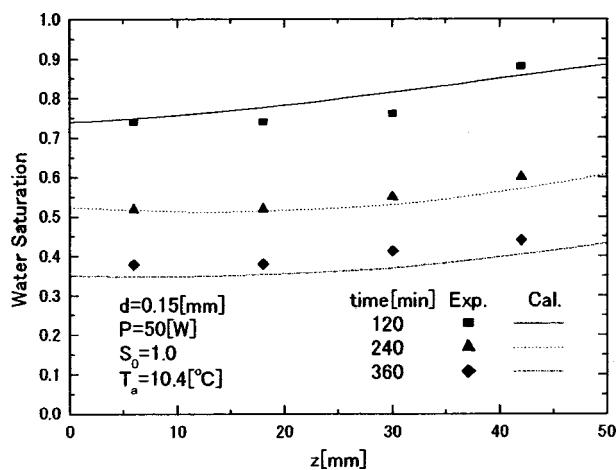


Fig. 13 Water saturation as a function of depth at various times ( $P=50$  W,  $d=0.15$  mm,  $s_0=1.0$ )

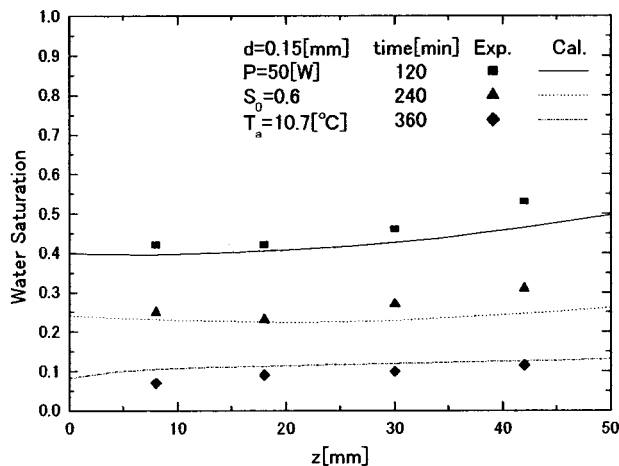


Fig. 14 Water saturation as a function of depth at various times ( $P=50$  W,  $d=0.15$  mm,  $s_0=0.6$ )

evaporating species. In this stage of drying, the capillary action plays an important role in the moisture migration mechanism, and maintains a good supply of liquid to the surface. Continued drying would cause the average moisture content inside the sample to decrease and leads to decrease microwave power absorbed (as referred to Fig. 10), reduced temperature (as referred to Fig. 7) and evaporation rate. Nevertheless, at the long stages of drying, the vapor diffusion effect plays an important role in the moisture migration mechanism because of the sustained vaporization that is generated within the sample. The simulated results are in agreement with the experimental results for microwave drying.

Figure 14 shows the average moisture profile along the sample depth in the case of  $s_0=0.6$ ,  $T_a=10.7^{\circ}\text{C}$ ,  $P=50$  W, and  $d=0.15$  mm. It is evident from the figure that the sample dries quickly throughout. In particular, the bulk of this sample that receives the largest amount of microwave power absorbed (which corresponds to a small initial moisture content) in the early stages of drying process, due to the penetration depth of the microwave field (as referred to Fig. 10).

The simulations of moisture distribution within the sample in the vertical plane ( $x$ - $z$ ) are shown in Fig. 15 and Fig. 16. It is seen that the moisture content now appears to be high close to side walls of the sample, and the moisture content at lowering edge of the sample stays higher due to the hydrodynamic properties.

The variation of drying rate with respect to time obtained by measurement is shown in Fig. 17. It is seen that in the early stages of drying, the drying rate of the sample in the case of small particle sizes is nearly the same in that case of large particle sizes. However, at long stages of drying, the observed drying rate of sample in the case of small particle sizes is higher than that

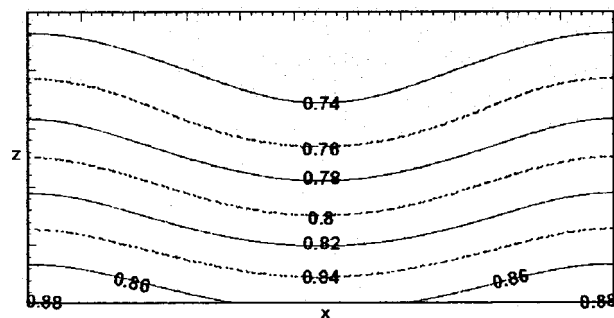


Fig. 15 The simulated water saturation distributions (dimensionless) within the sample ( $s_0=1.0$ , time=120 min,  $d=0.15$  mm, Dimensions: 110 mm ( $x$ )  $\times$  50 mm ( $z$ ))

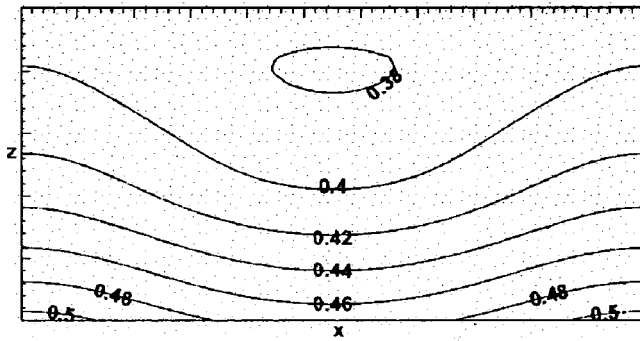


Fig. 16 The simulated water saturation distributions (dimensionless) within the sample, ( $s_0=0.6$ , time=120 min,  $d=0.15$  mm, Dimensions: 110 mm ( $x$ )  $\times$  50 mm ( $z$ ))

case of large particle sizes. This is because of the small particle sizes, however, leads to much higher capillary pressure resulting in a faster drying time.

**5.3 Microwave Drying of Two-Layered Porous Packed Bed.** Experimental results are shown in Figs. 18–21, which corresponds to that of  $s_0=1.0$ ,  $T_a=10.7^\circ\text{C}$ , and  $P=50$  W, along with the center axis ( $x=54.61$  mm) of rectangular waveguide. Figure 18 shows the moisture profile within F-C bed, from a macroscopic point of view for the hydrodynamic characteristic properties within two-layered porous packed bed, we will consider the liquid water transport at the interface between two beds where the

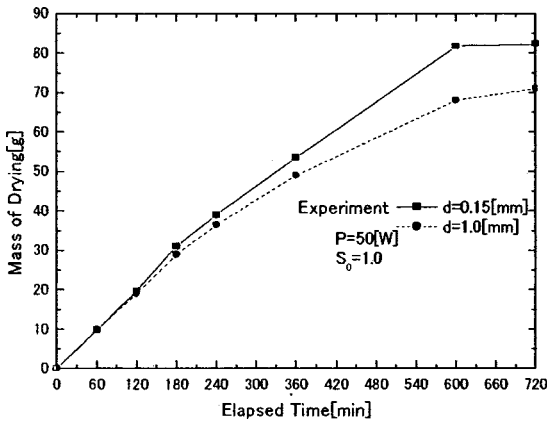


Fig. 17 The variation of drying rate with respect to time

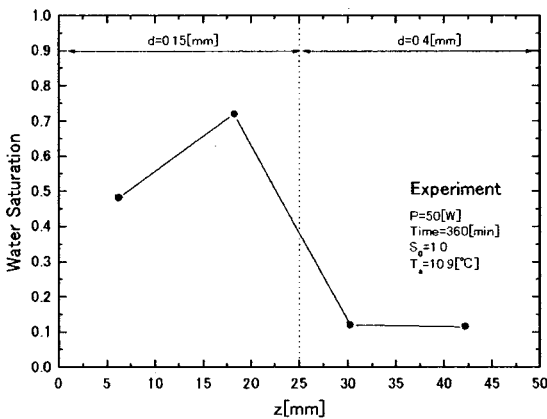


Fig. 18 water saturation as a function of depth for F-C Bed (Experiment:  $P=50$  W,  $t=360$  min)

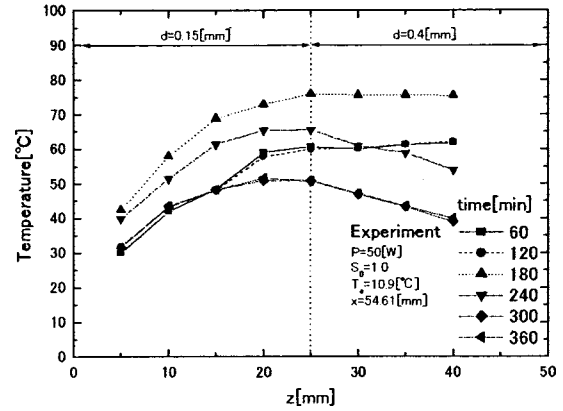


Fig. 19 Temperature as a function of depth at various times for F-C Bed (Experiment:  $P=50$  W,  $t=360$  min)

difference of particle size is considered during microwave drying. As referred to Fig. 3, in the case of the same capillary pressure, a small particle size corresponds to higher water content. Now, considering the case where two particle sizes having same capillary pressure and different particle sizes at the interface are justified. Since the capillary pressure has the same value at the interface between two beds, but the water saturation becomes discontinuous at the interface of two beds. This is because of the differences of the water characteristics between the two beds, the liquid water will be moved from the coarse bed to the fine bed (which corre

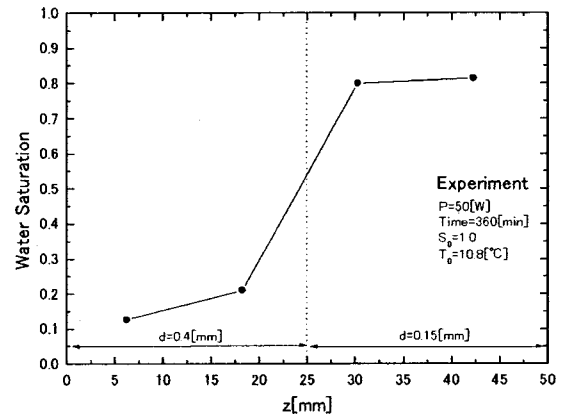


Fig. 20 water saturation as a function of depth for C-F Bed (Experiment:  $P=50$  W,  $t=360$  min)

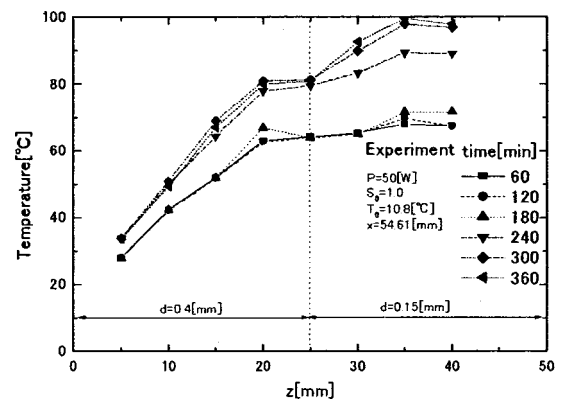


Fig. 21 Temperature as a function of depth at various times for C-F Bed (Experiment:  $P=50$  W,  $t=360$  min)

sponds to a higher capillary pressure) resulting in a faster drying time.

On the other hand, in the case of attaching fine bed under the coarse bed, called C-F bed is shown in Fig. 20. It is seen that the moisture content inside the fine bed displays very higher because a coarse bed set on the fine bed retards the upward migration of liquid water at the interface between two beds, while the moisture content inside the coarse bed stays lower due to the lower capillary pressure. Therefore, the efficiency of drying process in this case is the lowest.

The temperature profiles at various times and locations for both cases are shown in Fig. 19 and Fig. 21, respectively. Figure 19 shows that the temperature profile within the F-C bed rises up quickly in the early stages of drying process (about 10 min–60 min). However, its rise slows down after this stage. It is evident from the figure that near the end stages of drying as the moisture content inside the sample is reduced, this decreases the microwave power absorbed. Consequently, the temperature profiles are decreased in this stage of drying process. However, the temperature profile within the C-F bed (Fig. 21) corresponds to that of moisture content profile (as referred to Fig. 20) where the temperature continuously rises faster than that in the case of F-C bed. Further, the temperature remains high at the end of drying. This is because of a stronger standing wave with a larger amplitude is formed inside the C-F bed and having of dry layer-coarse bed (upper layer) protects the reflection of wave from the surface resulting in a higher rate of microwave power absorbed in the interior.

Additionally, microwave drying of C-F bed gives higher temperatures inside the fine bed (lower layer) while the temperature inside the coarse bed stays lower due to the behavior of the loss factor decreases significantly with decreasing moisture content and the cooling effect of surrounding air. The next steps in research in microwave drying of multi-layered porous packed bed are to develop a mathematical model for verifying the experimental data, and a study of the combined microwave and convective drying of capillary porous materials will be presented.

## 6 Conclusions

Experimental and predicted results of drying of capillary porous materials using a microwave energy as a heating source have been presented. The measurements of temperature and moisture distributions within the sample provide a good basis for understanding of the microwave drying process. The mathematical model gives qualitatively comparable trends to experimental data. The calculations of electromagnetic fields inside the rectangular waveguide and the sample show that the variation of particle sizes and initial moisture content changes the degree of penetration and rate of microwave power absorbed within the sample. Furthermore, the small particle size leads to much higher capillary pressure resulting in a faster drying time.

## Acknowledgment

The authors gratefully acknowledge the financial support provided under the Science Research Grant of the Japanese Ministry of Education, for the development of the experimental and simulated facilities described in this paper.

## Nomenclature

$B$	= magnetic flux density [Wb/m <sup>2</sup> ]
$C_p$	= specific heat capacity [J/kgK]
$D$	= electric flux density [C/m <sup>2</sup> ]
$D_0$	= binary mass diffusion coefficient [m <sup>2</sup> /s]
$d$	= diameter [m]
$d_p$	= deep of packed bed [m]
$E$	= electric field intensity [V/m]
$E_{yin}$	= the input value of electric field intensity [V/m]
$f$	= frequency of incident wave [Hz]
$g$	= gravitational constant [m/s <sup>2</sup> ]

$H$	= magnetic field intensity [A/m]
$h_c$	= heat transfer coefficient [W/m <sup>2</sup> K]
$h_m$	= mass transfer coefficient [m/s]
$H_v$	= specific heat of vaporization [J/kg]
$K$	= permeability [m <sup>2</sup> ]
$L_x$	= the length of waveguide in x-direction [m]
$\dot{n}$	= volumetric evaporation rate [kg/m <sup>3</sup> s]
$P$	= microwave power input [W]
$p$	= pressure [Pa]
$Q$	= microwave power absorbed term [W/m <sup>3</sup> ]
$q$	= heat flux [W/m <sup>2</sup> ]
$s$	= water saturation
$T$	= temperature [C]
$\tan \delta$	= loss tangent coefficient
$t$	= time [s]
$u, w$	= velocity [m/s]
$Z_H$	= wave impedance [ $\Omega$ ]
$Z_I$	= intrinsic impedance [ $\Omega$ ]

## Greek Letters

$\phi$	= porosity [m <sup>3</sup> /m <sup>3</sup> ]
$\rho$	= density [kg/m <sup>3</sup> ]
$\epsilon$	= complex permittivity [F/m]
$\epsilon'$	= dielectric constant [F/m]
$\epsilon''$	= dielectric loss factor [F/m]
$\lambda$	= free space wave length [m]
$\lambda_g$	= waveguide wave length [m]
$\lambda_{eff}$	= effective thermal conductivity [W/mK]
$\mu$	= magnetic permeability [H/m]
$\mu_g$	= dynamic viscosity of gas [Pa s]
$\mu_l$	= dynamic viscosity of liquid [Pa s]
$v$	= velocity of microwave [m/s]
$\sigma$	= electric conductivity [S/m]
$\xi$	= surface tension [Pa m]

## Subscripts

$\infty$	= ambient
$0$	= free space
$a$	= air
$c$	= capillary
$e$	= effective
$g$	= gas
$ir$	= irreducible
$n$	= component of normal direction
$p$	= particle
$r$	= relative
$t$	= component of tangent direction
$v$	= water vapor
$l$	= liquid water
$x, y, z$	= coordinates

## Superscripts

'	= interfacial position
---	------------------------

## References

- [1] Whitaker, S., 1977, "A Theory of Drying in Porous Media," *Adv. Heat Transfer*, **13**, pp. 119–203.
- [2] Feng, H., and Tang, J., 1998, "Microwave Finish Drying of Diced Apples in a Spouted Bed," *J. Food. Sci.*, **63**, No. 4, pp. 679–683.
- [3] Feng, H., Tang, J., and Cavalien, R. P., 1999, "Combined Microwave and Spouted Bed Drying of Diced Apples: Effect of Drying Conditions on Drying Kinetics and Product Temperature," *Drying Technol.*, **17**, No. 10, pp. 1981–1998.
- [4] Constant, T., Moyné, C., and Perre, P., 1996, "Drying with Internal Heat Generation: Theoretical Aspects and Application to Microwave Heating," *AIChE J.*, **42**, No. 2, pp. 359–368.
- [5] Metaxas, A. C., and Meredith, R. J., 1983, *Industrial Microwave Heating*, Peter Peregrinus, Ltd., London.
- [6] Ayappa, K. G., Davis, H. T., Davis, E. A., and Gordon, J., 1991, "Analysis of Microwave Heating of Materials with Temperature-Dependent Properties," *AIChE J.*, **37**, No. 3, pp. 313–322.
- [7] Li, W., Ebadian, M. A., White, T. L., and Grubb, R. G., 1993, "Heat Transfer

- Within a Concrete Slab Applying the Microwave Decontamination Process,” *ASME J. Heat Transfer*, **115**, pp. 42–50.
- [8] Clemens, J., and Saliel, C., 1996, “Numerical Modeling of Materials Processing In Microwave Furnaces,” *Int. J. Heat Mass Transf.*, **39**, No. 8, pp. 1665–1675.
- [9] Gori, F., Gentili, G., and Matini, L., 1987, “Microwave Heating of Porous Media,” *ASME J. Heat Transfer*, **109**, pp. 522–525.
- [10] Perkin, R. M., 1980, “The Heat and Mass Transfer Characteristics of Boiling Point Drying Using Radio Frequency and Microwave Electromagnetic Fields,” *Int. J. Heat Mass Transf.*, **23**, pp. 687–695.
- [11] Turner, W., and Ilic, M., 1991, “Combined Microwave and Convective Drying of a Porous Material,” *Drying Technol.*, **9**, No. 5, pp. 1209–1269.
- [12] Ayappa, K. G., Davis, H. T., Crapiste, G., Davis, E. A., and Gordon, J., 1991, “Microwave Heating: An Evaluation of Power Formulations,” *Chem. Eng. Sci.*, **46**, No. 4, pp. 1005–1016.
- [13] Ratanadecho, P., Aoki, K., and Akahori, M., 2001, “Experimental and Numerical Study of Microwave Drying in Unsaturated Porous Material,” *Int. Commun. Heat Mass Transfer*, **28**, No. 5, pp. 605–616.
- [14] Aoki, K., Ratanadecho, P., and Akahori, M., 2000, “Characteristics of Microwave Heating for Multi-layered Materials Using a Rectangular Wave Guide,” *Proceeding of the 4th JSME-KSME Thermal Engineering Conference*, October 1–6, Kobe, Japan, Vol. 2, pp. 191–196.
- [15] Ratanadecho, P., Aoki, K., and Akahori, M., 2002, “A Numerical and Experimental Study of Microwave Melting of Frozen Packed Bed Using a Rectangular Wave Guide,” *IEEE Trans. Microwave Theory Tech.*, accepted for publication.
- [16] Perre, P., and Turner, W., 1997, “Microwave Drying of Softwood in an Oversized Waveguide,” *AIChE J.*, **43**, No. 10, pp. 2579–2595.
- [17] Wang, J., and Schmutge, T., 1980, “An Empirical Model for the Complex Dielectric Permittivity of Soil as a Function of Water Content,” *IEEE Trans. Geosci. Remote Sens.*, **GE-18**, No. 4, pp. 288–295.
- [18] Mur, G., 1981, “Absorbing Boundary Conditions for the Finite-Difference Approximation of the Time-Domain Electromagnetic-Field Equations,” *IEEE Trans. Electromagn. Compat.*, **EMC-23**, No. 4, pp. 377–382.
- [19] Bories, S. A., 1991, “Fundamental of Drying of Capillary-Porous Bodies,” in Kakac, S., Kilkis, B., Kulacki, F. and Arinc, F. eds., *Convective Heat and Mass Transfer in Porous Media*, NATO ASI series, Vol. 196, Kluwer Publishers, pp. 39–434.
- [20] Kaviany, M., 1991, *Principle of Heat Transfer in Porous Media*, Springer, New York.
- [21] Kaviany, M., and Mittal, M., 1987, “Funicular State in Drying of Porous Slab,” *Int. J. Heat Mass Transf.*, **30**, No. 7, pp. 1407–1418.
- [22] Aoki, K., Hattori, M., Kitamura, M., and Shiraishi, N., 1991, “Characteristics of Heat Transport in Porous Media With Water Infiltration,” *ASME/JSME Thermal Engineering Proceedings*, Vol. 4, pp. 303–308.
- [23] Patankar, S. V., 1980, *Numerical Heat Transfer and Fluid Flow*, Hemisphere Publishing Corporation, New York.
- [24] Feng, H., Tang, J., and Cavalien, R. P., 2001, “Dielectric Properties of Dehydrated Apples as Affected by Moisture and Temperature,” *Trans. ASAE*, (in press).
- [25] Von Hippel, A. R., 1954, *Dielectric Materials and Applications*, MIT Press, Boston.